CHAPTER 3
NUMERICAL RESULTS ON THE WIDE BAND GAP SEMICONDUCTORS

In this chapter, we present optical response studies of the wide band gap semiconductors including four polytypes of SiC (3C, 2H, 4H, and 6H), BN, AlN, and GaN. We choose to study these binary compounds not only because of their importance in industrial applications but also because of their simple structures – zincblende, wurtzite and other hexagonal structures. The d electrons, which may introduce additional complications, are not present in most of these materials with the exception of GaN. A significant amount of effort is spent on studying the effects of the scissors operators in these wide gap materials. We will find that, contrary to the success in small to medium gap materials, using the scissors operators in the wide gap materials gives predictions of optical response coefficients too small compared to experiment. Using our calculated second-harmonic susceptibilities on these simple σ-bonded compounds, we can test the validity of bond-additivity. Bond-additivity is a basic assumption of the semiclassical models that allows adding the hyperpolarizabilities of individual bonds in a crystal to obtain the macroscopic second-harmonic susceptibility. Optical response coefficients can depend sensitively on the pseudopotentials, we take care in constructing and testing the pseudopotentials we use. The local-field corrections to the second-harmonic susceptibilities are recalculated by including the nonlinear local field for most of the materials we have studied.* The results we present here are somewhat different from those given in earlier publications[4] because of the different choices of the pseudopotentials.

3.1 Pseudopotentials

Our calculations use plane-waves as basis functions implemented with pseudopotentials. Since the calculated optical response coefficients depend sensitively on both the valence and conduction bands, it is important to use pseudopotentials that give similar scattering properties as the all-electron potentials over a wide energy range. We choose norm-conserving[5] pseudopotentials with double-reference[6] Kleinman-Bylander[7] type projection operators and nonlinear core corrections.[8] In this section, we describe the various features of the pseudopotentials and results on testing the pseudopotentials.

3.1.1 Description of the pseudopotentials

Pseudopotentials are constructed to replace the oscillating part of the valence electron wavefunctions close to the core by a smooth function while preserving the wavefunction at and beyond the bonding region. First a LDA calculation on an isolated atom gives a self-consistent all-electron potential $V^{AE}(r)$ and the wave-

* We exclude urea,[1] α-quartz,[2] and SiGe for our current study because of the rather large system sizes for the first two cases, and the importance of the Ge-3d electrons in SiGe.[3]

functions $u_l^{AE}(r)$ with eigenvalue ϵ_l,

$$\left[-\frac{1}{2}\frac{d^2}{dr^2}+\frac{l(l+1)}{2r^2}+V^{AE}(r)\right]u_l^{AE}(r)=\epsilon_l u_l^{AE}(r), \tag{3.1}$$

in which $u_l(r)=rR_l(r)$ where $R_l(r)Y_{lm}(\hat{r})$ is the eigenfunction (the principle quantum number is suppressed because we focus on the valence electrons). The pseudopotentials $V_l^{psp}(r)$ and pseudo-wavefunctions $u_l^{psp}(r)$ are constructed to satisfy the Schroedinger equation at the same energy ϵ_l as the all-electron calculation,

$$\left[-\frac{1}{2}\frac{d^2}{dr^2}+\frac{l(l+1)}{2r^2}+V_l^{psp}(r)\right]u_l^{psp}(r)=\epsilon_l u_l^{psp}(r). \tag{3.2}$$

Beyond a matching radius r_c chosen outside the core region, the pseudopotentials and pseudo-wavefunctions match onto the all electron potential and all-electron wavefunctions. Inside r_c, the all electron potential and wavefunctions are replaced by smooth functions which have lower Fourier components.[9]

Norm-conserving pseudopotentials. There are different schemes of constructing the pseudopotentials.[9] We use the method by Troullier and Martin[10] which has the following features:

$$\begin{array}{lll}
(1)\ u_l^{psp}(r)=u_l^{AE}(r),\quad V_l^{psp}(r)=V^{AE}(r), & & \text{for}\quad r>r_c,\\
(2)\ \dfrac{d^n u_l^{psp}(r)}{dr^n}=\left.\dfrac{d^n u_l^{AE}(r)}{dr^n}\right|_{r=r_c}, & & n=1,2,3,4,\\
(3)\ \left.\dfrac{d^2 u_l^{psp}(r)}{dr^2}\right|_{r=0}=0 & & \text{smoothness condition},\\
(4)\ \displaystyle\int_0^{r_c}dr[u_l^{psp}(r)]^2=\int_0^{r_c}dr[u_l^{AE}(r)]^2, & & \text{norm-conserving condition.}
\end{array} \tag{3.3}$$

The first condition forces the pseudo wavefunctions and pseudopotentials to be identical to the all-electron wavefunctions and potential outside r_c. The second condition requires the four radial derivatives of the pseudo wavefunctions at r_c to be equal to those of the all-electron wavefunctions. The smoothness condition was tested[10] to give pseudopotentials with low Fourier components. The norm-conserving condition states that the pseudo-wavefunction has the same normalization inside the matching radius, which condition leads to similar scattering properties[5] of the pseudopotential as the all-electron potential near the reference energy ϵ_l. The scattering property can be measured in terms of the phaseshifts of the partial waves defined later in this section. The pseudopotentials and pseudo-wavefunctions thus constructed for nitrogen are shown in Figure 3.1.

Kleinman-Bylander type pseudopotentials. Since the pseudopotentials for different angular momentum component l's are different inside r_c, there are various ways to represent this l-dependence. In the original applications,[5] pseudopotentials are written in the so-called "semi-local" form

$$\begin{aligned} V^{psp} &= V_{loc}(r) + V_{semi-loc} \\ &= V_{loc}(r) + \sum_l |l\rangle v_l(r) \langle l|, \\ v_l(r) &= V_l^{psp}(r) - V_{loc}(r), \end{aligned} \tag{3.4}$$

where $|l\rangle\langle l|$ is the projection operator onto the lth angular component. The local potential $V_{loc}(r)$ is usually chosen[5] to be the same as one of the $V_l^{psp}(r)$, say with $l = 2$. The semilocal part of the pseudopotential is local in its radial dependence and nonlocal in its angular dependence. In solid state calculations, the Fourier transforms of the pseudopotentials are needed. In the case of semi-local pseudopotentials, the Fourier transformation requires $N_{pw}^2/2$ (N_{pw} is the number of plane-waves) number of numerical integrations to evaluate numerically, which can become a bottle-neck for large calculations. Kleinman-Bylander[7] proposed a form of fully-separable pseudopotentials that give similar scattering properties as the

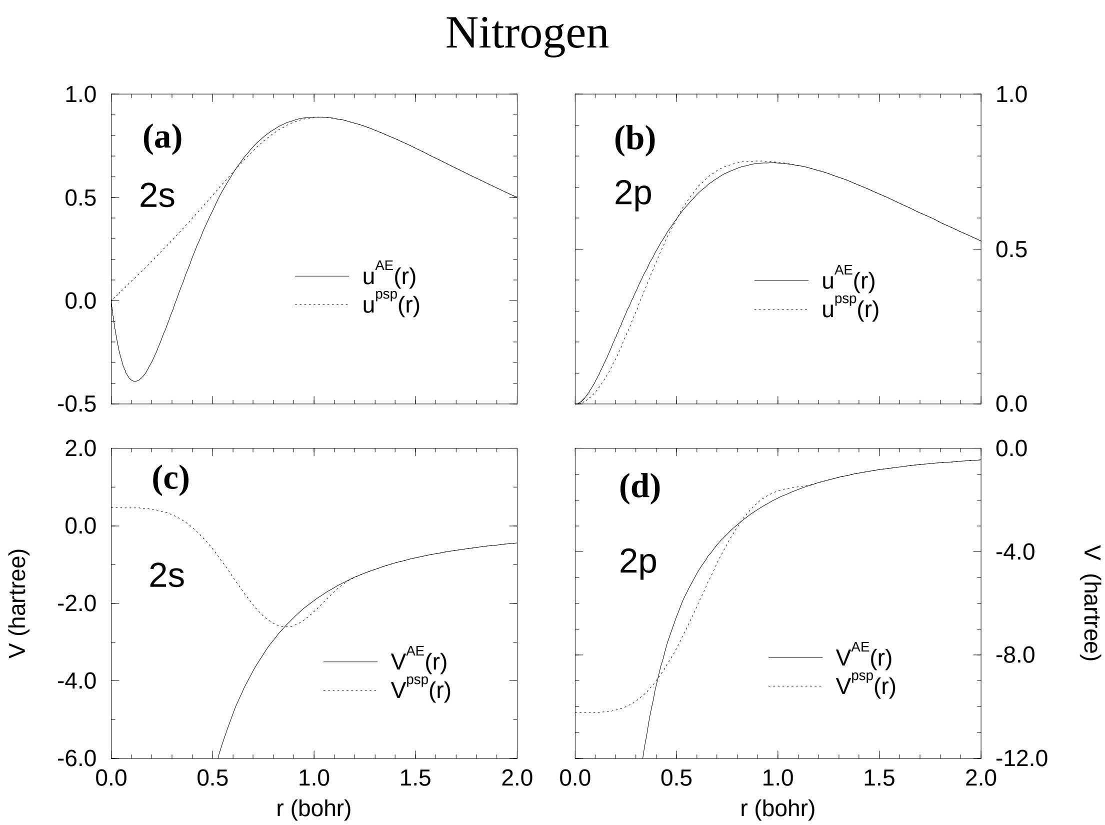

FIGURE 3.1 Pseudo wavefunctions and pseudopotentials for nitrogen. In figs. (a) and (b), the 2s and 2p pseudo wave-functions $u^{psp}(r)$ match onto the all-electron wavefunctions $u^{AE}(r)$ at the radii of 1.40 bohr and 1.58 bohr, respectively. For each partial wave, the pseudo wavefunction and its four derivatives are constructed to be equal to those of the atomic wavefunction at the matching radius. After obtaining the pseudo wavefunctions, the pseudopotentials $V^{psp}(r)$, shown in figs. (c) and (d), can be constructed from the Schroedinger equation Eq. (3.2).

semilocal pseudopotential and at the same time reduce the number of integrations to N_{pw},

$$\begin{aligned} V^{psp} &= V_{loc}(r) + V_{K-B} \\ &= V_{loc}(r) + \sum_l |l\rangle |u_l^{psp} v_l\rangle \epsilon_{K-B}^{-1} \langle u_l^{psp} v_l | \langle l|, \end{aligned} \tag{3.5}$$

where $\epsilon_{K-B} = \langle u_l^{psp} | v_l | u_l^{psp} \rangle$. In V_{K-B}, both the radial dependence $|u_l^{psp} v_l\rangle\langle u_l^{psp} v_l|$ and angular dependence $|l\rangle\langle l|$ are projection operators so V_{K-B} is fully nonlocal.

Double-reference projection operators. For Kleinman-Bylander type pseudopotentials, unphysical "ghost states" with energies lower than the ground state energy ϵ_l can appear[11] when the wavefunctions are almost orthogonal to the projector $|u_l^{psp} v_l\rangle$. Blochl suggested using multiple projection operators in Eq. (3.5) to lift the ghost states to higher energies.[6] In practice, two projection operators are sufficient with one being the original projection operator and the second one chosen to match the phaseshift of the semilocal pseudopotential at about one hartree above the first reference energy ϵ_l. The phaseshift of a partial wave with energy ϵ is defined by

$$\text{phase-shift} \equiv \tan^{-1}\left[\frac{du_l(\epsilon, r)/dr}{u_l(\epsilon, r)}\right], \tag{3.6}$$

The wavefunctions $u_l(\epsilon, r)$, which are not necessarily eigenstates, are chosen to approach the origin as r^{l+1} and satisfy Eqs. (3.1) and (3.2) for the all-electron potential and the pseudopotentials, respectively. As shown in Figure 3.2, the phaseshifts of the semi-local pseudopotential, single-reference and double-reference Kleinman-Bylander type pseudopotentials reproduce the phaseshifts of the all-electron potential in nitrogen up to four hartree above the eigenvalue, which is sufficient for our optical calculations.

Nonlinear core corrections (NLCC). In solid calculations, "ionic" pseudopotentials are needed with the screening of the electrons subtracted from $V_l^{psp}(r)$.

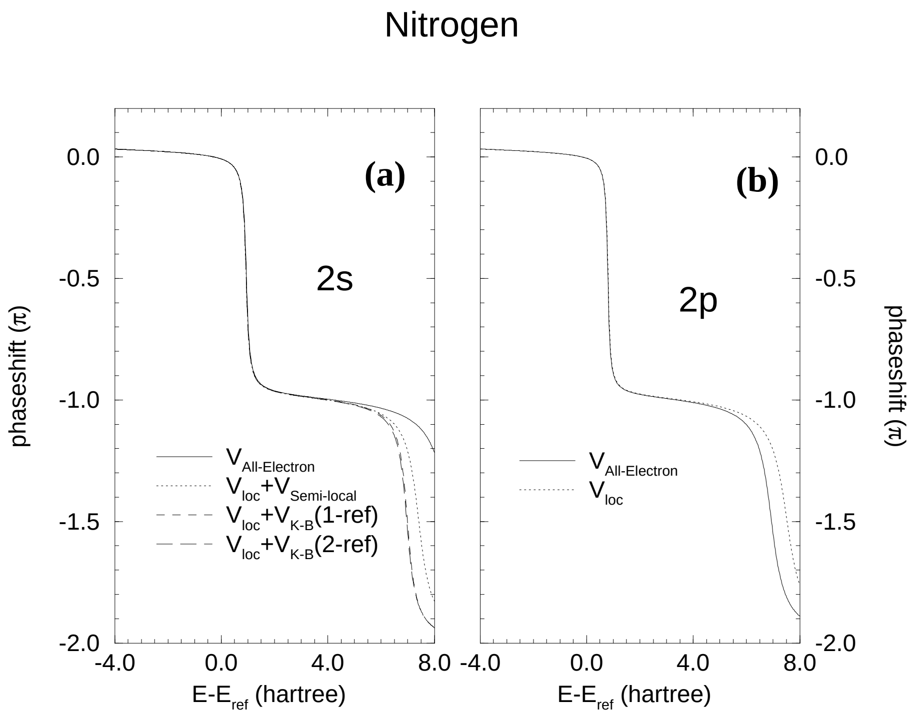

FIGURE 3.2 Phaseshifts of various pseudopotentials compared with the all-electron (or atomic) potential in nitrogen for states 2s, fig. (a), and 2p, fig. (b). The reference energies E_{ref} are chosen to be the eigenenergies of the atomic 2s and 2p states. The 2p pseudopotential is taken to be the local pseudopotential. The pseudopotentials reproduce the phaseshifts of the all-electron potentials up to 4 hartree – which is sufficiently accurate for LDA and optical response calculations. For the state 2s, the local pseudopotential plus the double-reference Kleinman-Bylander type pseudopotential [$V_{loc}+V_{K-B}$(2-ref)] is used in our LDA and optical calculations.

Since the amount of unscreening is the same for all partial waves, the change to the pseudopotentials can be included in the local part on which we now focus. If the charge density for the atomic core electrons is $\rho_c^A(r)$ and the charge density of the pseudo valence electrons is $\rho_v^{A,psp}(r)$, we tentatively unscreen the pseudopotential from both the core and the pseudovalence charge densities to obtain an ionic pseudopotential $\overline{V}_{loc}^{ion}(r)$,

$$\overline{V}_{loc}^{ion}(r) \equiv V_{loc} - \int d^3r' \frac{\rho_v^{A,psp}(r') + \rho_c^A(r')}{|\vec{r} - \vec{r}\,'|} - V_{xc}[\rho_v^{A,psp}(r) + \rho_c^A(r)], \tag{3.7}$$

where $V_{xc}[\rho(r)]$ is the exchange-correlation potential. The functional form of $V_{xc}[\rho(r)]$ is nonlinear in the density $\rho(r)$, e.g., in the X_α approximation $V_{xc}[\rho] = X_\alpha \rho^{-1/3}$, where X_α is a constant.[12] In solids, the core electrons are assumed to be frozen in the atomic configuration and hence the core charge density of the solid $\rho_c^S(r)$ is equal to that of the atom, i.e., $\rho_c^S(r) = \rho_c^A(r) \equiv \rho_c(r)$. Taking the valence charge density in solid to be $\rho_v^S(\vec{r})$, the potential seen by the electrons in the solid is

$$\begin{aligned}
V(r) =& \overline{V}^{ion}(r) + \int d^3r' \frac{\rho_v^S(\vec{r}\,') + \rho_c(r')}{|\vec{r} - \vec{r}\,'|} + V_{xc}[\rho_v^S(\vec{r}) + \rho_c(r)] \\
=& V_{loc}(r) - \int d^3r' \frac{\rho_v^{A,psp}(r') + \rho_c(r')}{|\vec{r} - \vec{r}\,'|} - V_{xc}[\rho_v^{A,psp}(r) + \rho_c(r)] \\
&+ \int d^3r' \frac{\rho_v^S(\vec{r}\,') + \rho_c(r')}{|\vec{r} - \vec{r}\,'|} + V_{xc}[\rho_v^S(\vec{r}) + \rho_c(r)] \\
=& V_{loc} - \int d^3r' \frac{\rho_v^{A,psp}(\vec{r}\,')}{|\vec{r} - \vec{r}\,'|} - V_{xc}[\rho_v^{A,psp}(r) + \rho_c(r)] \\
&+ \int d^3r' \frac{\rho_v^S(\vec{r}\,')}{|\vec{r} - \vec{r}\,'|} + V_{xc}[\rho_v^S(\vec{r}) + \rho_c(r)] \\
=& V^{ion}(r) + \int d^3r' \frac{\rho_v^S(\vec{r}\,')}{|\vec{r} - \vec{r}\,'|} + V_{xc}[\rho_v^S(\vec{r}) + \rho_c(r)]
\end{aligned} \tag{3.8}$$

where the new ionic pseudopotential is

$$V^{ion}(r) \equiv V_{loc} - \int d^3r' \frac{\rho_v^{A,psp}(\vec{r}\,')}{|\vec{r} - \vec{r}\,'|} - V_{xc}[\rho_v^{A,psp}(r) + \rho_c(r)]. \tag{3.9}$$

Unlike $\overline{V}^{ion}(r)$, the newly defined ionic pseudopotential $V^{ion}(r)$ is much softer because the Coulomb potential of the core charges is not unscreened. Using Eqs. (3.9) and (3.8) to unscreen the pseudopotential and calculating the potential in solid is called including the nonlinear core corrections, denoted by NLCC.[8] The atomic core charge density is used when unscreening the exchange-correlation potential and is used again in the solid to add to the valence density when calculating the exchange-correlation potential. The reason for explicitly keeping the core charge is that, unlike the Coulomb potential, the exchange-correlation potential is nonlinear in its dependence on the density, and hence is not additive.

In cases where the core charge and valence charge densities are completely separated in space, the following approximation can be made

$$V_{xc}[\rho_c(r) + \rho_v(r)] \approx V_{xc}[\rho_c(r)] + V_{xc}[\rho_v(r)], \tag{3.10}$$

and an ionic pseudopotential can be chosen as

$$\tilde{V}_{ion}(r) \equiv V_{loc} - \int d^3r' \frac{\rho_v^{A,psp}(\vec{r}\,')}{|\vec{r} - \vec{r}\,'|} - V_{xc}[\rho_v^{A,psp}(r)]. \tag{3.11}$$

In the solid calculation, the potential is changed accordingly:

$$V(r) = \tilde{V}_{ion}(r) + \int d^3r' \frac{\rho_v^{S}(\vec{r}\,')}{|\vec{r} - \vec{r}\,'|} + V_{xc}[\rho_v^{S}(\vec{r})]. \tag{3.12}$$

Using Eqs. (3.11) and (3.12) completely eliminates the core-charge density in the solid calculation. However, since Eq. (3.10) is not usually a good approximation, excluding NLCC [i.e., using Eqs. (3.11) and (3.12)] is not as accurate as including NLCC [i.e., using Eqs. (3.8) and (3.9)]. As shown in Figure 3.3, there is a significant overlap of the valence and core charge densities even in silicon where the core electrons are tightly bound to the nucleus. Further tests given in the next subsection show that only by including NLCC do we obtain consistent results on lattice constant calculations. We will use the nonlinear core-charge corrections in all our studies unless otherwise specified.

3.1.2 Testing pseudopotentials

Phaseshifts. As a first test of the pseudopotentials, we compare the phaseshifts of the pseudopotentials to those of the all-electron potential. An example is given for the 2s and 2p states of nitrogen in Figure 3.1. In all the cases we have studied, the phaseshifts of the pseudopotentials follow the phaseshifts of all electron potentials at least up to 1 hartree above the reference energy. Double-reference[6] Kleinman-Bylander[7] pseudopotentials give, in most cases, better phaseshifts than single-reference pseudopotentials.

Large cell calculations with a single atom. As a second test of the pseudopotentials, we carry out a large simple cubic cell with a single atom placed at the center of the cell. The lattice constants, which we take to be 12-15 bohr, are much larger than typical atomic spacings in solids. Plane-waves and pseudopotentials are used in these calculations. If the pseudopotentials are good representations of the all electron potential, the ground state of the atom in the large cell should be very close to an isolated atom. To test this, we compare the difference between the splittings of the valence state energies of the atom in the large cell calculation and the original atomic calculation. The agreement is good as shown in Table 3.1.

Lattice constant. As a third test, we calculate the LDA lattice constants using the pseudopotentials. In Table 3.2, we compare the lattice constants of experiments with those determined by LDA obtained with two methods: (1) plane-wave

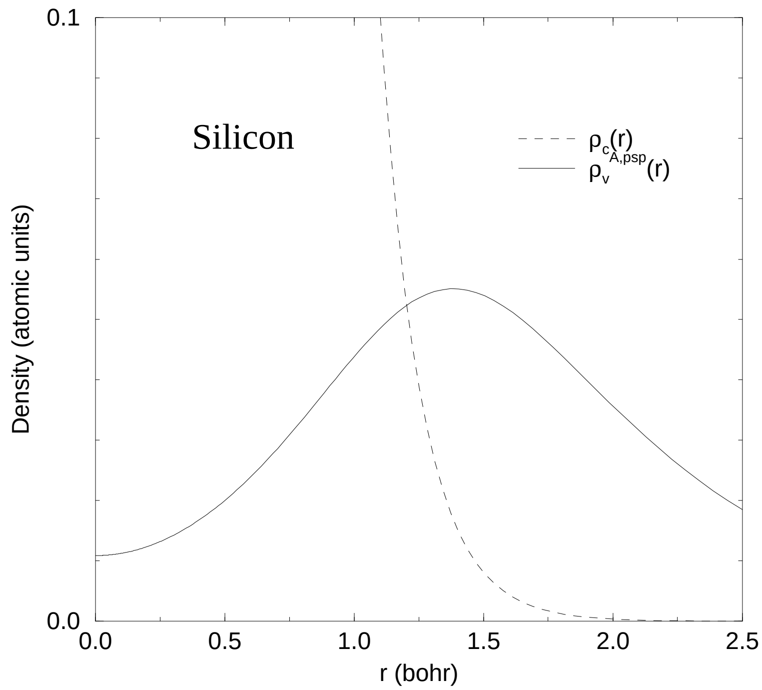

FIGURE 3.3 The core charge density $\rho_c(r)$ and the pseudo valence charge density $\rho_v^{A,psp}(r)$ of the silicon atom. There is a significant overlap of the two charge densities near $r = 1.2$ bohr. It is a poor approximation to separate the exchange-correlation potential into a purely valence part contribution and a purely core part: $V_{xc}[\rho_v^{A,psp}(r) + \rho_c(r)] \approx V_{xc}[\rho_v^{A,psp}(r)] + V_{xc}[\rho_c(r)]$, as done in calculations without nonlinear core corrections. The correct procedure in a solid calculation is to add the core charge density of the atom to the valence charge density of the solid when computing the exchange-correlation potential. At the same time, the pseudopotential has to be unscreened with the core charge density included when subtracting the exchange-correlation potential. The procedure is given in Eq. (3.8) and (3.9) in the text.

TABLE 3.1 Eigenenergy difference between the highest filled p and s orbitals from two separate calculations: (1) large cell calculations using pseudopotentials with an atom placed in a simple cubic cell repeated in space; (2) all electron calculation of an isolated atom. In the large cell calculation, the lattice constant is chosen between 12-15 bohr – much larger than typical atomic spacing in solids. Two $\vec{k}$-points are used in these calculations. The eigenvalue difference between the two $\vec{k}$-points is less than 0.01 eV, which shows that the lattice size is large enough to suppress atomic-atomic interactions. The agreement between the two calculations shows that the pseudopotentials are good representations of the atomic potentials. Units are in eV.

	B	Al	Ga	In	C	Si	Ge	N	P	As	O	S	Se
$\Delta E_{large-cell}$	5.7	5.0	6.4	5.8	8.2	6.7	7.9	11.2	8.4	9.4	14.6	10.2	10.8
ΔE_{atom}	5.7	5.0	6.4	5.7	8.4	6.7	7.8	11.2	8.3	9.3	14.6	10.1	10.8

pseudopotential calculations and (2) full-potential linear augmented plane-wave (FLAPW) calculations. The latter is an "all-electron" calculation in which the core charge density relaxes in the solid potential. The two LDA determined lattice constants agree with each other and both agree with experiment to 1.5%. An exception is the GaN plane-wave pseudopotential calculation. In this particular case, the 3d electrons of Ga mixes with the 2s electrons of N in the solid. Freezing the 3d electrons in the core produces a slightly worse lattice constant which is 2.5% smaller than the experimental value. To take the 3d electrons into account, we carry out a separate calculation with the 3d electrons in the valence states and we obtain an improved lattice constant which is 0.6% smaller than experiment.

To demonstrate the effect of the NLCC, we carry out two sets of calculations for

TABLE 3.2 LDA lattice constant (a) calculations for diamond and zincblende structures using plane-wave pseudopotentials (psp) and full potential linear augmented plane-waves (FLAPW) compared with experimental values. The error is defined as $100\% \times (a_{LDA} - a_{Exp})/a_{Exp}$. Both LDA calculations agree with experiment to 1.5%, with the exception of the GaN calculation using plane-wave pseudopotentials where the error is -2.5%. In a separate calculation listed as GaN (3d), by including the 3d electrons in the valence bands leads to much improved lattice constant with the error of -0.6%. The reason for this improvement is that the 3d electrons of Ga hybridize with the 2s electrons of N and should no longer be treated as core. In both pseudopotential and FLAPW calculations, six to ten lattice constants are used around the experimental value. The total energy of these calculations are spline fit to a quadratic form to determine the lattice constant that gives the minimum total energy. Units for the lattice constants are in bohr.

	plane-wave psp		FLAPW		Exp.
	a_{LDA}	error	a_{LDA}	error	a_{Exp}
C	6.70	−0.8%	6.69	−0.09%	6.75
Si	10.21	−0.5%	10.22	−0.04%	10.26
Ge	10.57	−1.1%	10.61	−0.6%	10.69
BN	6.80	−0.5%	6.78	−0.7%	6.83
AlN	8.23	−0.6%	8.22	−0.8%	8.28
GaN	8.33	−2.5%	8.43	−1.2%	8.54
GaN (3d)	8.49	−0.6%			8.54
InN	9.29	−1.3%	9.34	−0.8%	9.41
AlP	10.29	−0.1%	10.27	−0.3%	10.30
AlAs	10.62	0.0%	10.64	+0.2%	10.62
GaP	10.18	−1.5%	10.19	−1.4%	10.34
GaAs	10.53	−1.5%	10.59	−0.9%	10.69
SiC	8.20	−0.5%	8.20	−0.5%	8.24

the LDA lattice constants of the III-V nitrides (BN, AlN, GaN, and InN) each with and without the NLCC: (1) Pseudopotentials generated with the atomic configuration of valence electrons in the ground state, i.e., III: s^2p^1, V: s^2p^3; (2) pseudopotentials generated with valence electrons in the sp^3 configuration, i.e., III: $s^{0.75}p^{2.25}$, V: $s^{1.25}p^{3.75}$. If the pseudopotentials are "transferable", the pseudopotentials generated using different valence electron configurations should give basically the same lattice constants. In our test cases shown in Table 3.3, the lattice constants obtained with NLCC barely changed with the pseudopotentials generated using different atomic configurations. In contrast, the lattice constants obtained without NLCC differ by 2-5% with different atomic configurations in the pseudopotential generation. This study demonstrates the importance of NLCC in calculations using pseudopotentials. Since inclusion of the NLCC does not pose any numerical difficulty, they should be included in all pseudopotential calculations, even for first and second row elements.

Band structures. As a fourth test of the pseudopotentials, we compare our calculated band structures with calculations using other methods and published results of other research groups. Within an error range of 0.3 eV, our calculated band structures for zincblende SiC, BN, AlN, and GaN agree with results of the FLAPW calculations and with the results in literature.[13,14,15] Comparison of the LDA band structures with the quasi-particle band structure obtained using the "GW" approximation[13,14,15] gives the "scissors" shift we use in the subsequent optical response calculations. We obtain the value of the scissors shift by taking the difference between the band gaps of LDA and GW calculations with an equaly weighted average over the $\vec{k}$-points Γ, X, and L.

TABLE 3.3 LDA lattice constant calculations for the zincblende structures of the III-V nitrides using pseudopotentials with and without nonlinear core corrections (NLCC). The pseudopotentials are generated with two different atomic configurations of the valence electrons. In the "atomic" configuration, the ground state is used: III, s^2p^1; V, s^2p^3. The "sp^3" calculations are motived by the s-p^3 hybridization in these σ-bonded systems. The configuration of the valence electrons for the sp^3 calculations are: III, $s^{0.75}p^{2.25}$; V, $s^{1.25}p^{3.75}$. In the calculations without NLCC, the lattice constants charge by 2-5% with different atomic configurations, 3% in BN with only first row elements. In the calculations with NLCC, the lattice constants barely change with pseudopotentials generated using different atomic configurations. These calculations demonstrate the importance of the NLCC, even in first and second row elements. Units are in bohr.

	without NLCC		with NLCC		Exp.
Config.	atomic	sp^3	atomic	sp^3	
BN	6.96	6.79	6.79	6.80	6.83
AlN	8.30	8.13	8.23	8.23	8.28
GaN	8.41	7.98	8.32	8.33	8.54
InN	8.70	8.45	9.34	9.29	9.41

TABLE 3.4 Comparison of the band structures of zincblende SiC, BN, AlN, GaN obtained from LDA and GW calculations and experimental values. The energy at the top of the valence band at Γ point is set to zero. The present calculation uses plane-waves and pseudopotentials with nonlinear core corrections. We did a separate LDA calculation using full-potential linear augmented plane-waves. In the SiC calculation, Ref. 13 uses pseudopotentials and gaussian orbitals as basis functions. In BN, AlN, and GaN, Ref. 14 and Ref. 15 both use plane-waves and pseudopotentials. The agreement between the LDA calculations is in most case within 0.1 eV but can sometimes differ by 0.3 eV. The GW calculations give good band structures compared with experiment. To obtain the scissors shift for our optical calculations, we take the difference between the gaps of GW and the present LDA calculations averaged over Γ, X, and, L with equal weight. The scissors shift obtained in this way are: SiC 1.3 eV, BN 2.5 eV, AlN 2.0 eV, and GaN 1.5 eV.

SiC	Γ_c	X_v	X_c	L_v	L_c	BN	Γ_c	X_v	X_c	L_v	L_c
LDA[a]	6.1	−3.2	1.2	−1.1	5.2	LDA[a]	8.7	−4.9	4.4	−1.9	10.1
LDA[b]	6.1	−3.2	1.3	−1.1	5.4	LDA[b]	8.7	−4.9	4.4	−1.9	10.2
LDA[c]	6.4	−3.2	1.3	−1.1	5.5	LDA[d]	8.6	−4.9	4.3	−1.9	10.1
GW[c]	7.3	−3.6	2.3	−1.2	6.5	GW[d]	11.4	−5.5	6.3	−2.2	12.4
Exp[c]		−3.6	2.4	−1.2	4.2	Exp[d]	14.5		6.1		
AlN	Γ_c	X_v	X_c	L_v	L_c	GaN	Γ_c	X_v	X_c	L_v	L_c
LDA[a]	4.1	−1.8	3.2	−0.5	7.1	LDA[a]	1.9	−2.4	3.3	−0.8	4.7
LDA[b]	4.1	−1.8	3.2	−0.5	7.2	LDA[b]	1.7	−2.7	3.3	−1.0	4.4
LDA[e]	4.2	−1.8	3.2	−0.5	7.3	LDA[e]	2.1	−2.8	3.2	−1.0	5.0
GW[e]	6.0	−2.1	4.9	−0.6	9.3	GW[e]	3.1	−1.1	6.2	−3.0	4.7
						Exp[f]	3.3				

[a] Present LDA calculations using plane-wave pseudopotentials.

[b] Our LDA calculations using full-potential linear augmented plane-waves.

[c] Ref. 13. [d] Ref. 14. [e] Ref. 15. [f] Ref. 16.

Optical response. As a final test of the pseudopotentials, we calculate the dielectric constants and the second-harmonic susceptibilities using two types of pseudopotentials: norm-conserving and hardness-conserving.[17] The hardness-conserving pseudopotentials are constructed to have the same hardness η

$$\eta \equiv \frac{\partial \mu}{\partial n} = \frac{\partial^2 E}{\partial n^2} \tag{3.13}$$

as the atomic potential. Hardness-conserving pseudopotentials[17] give a better description of charge transfer in molecules and solids. However, the disadvantage is that they are deeper and require much higher energy cutoffs for the calculations using plane-waves. We carry out two independent calculations with the same LDA and optical response codes with different pseudopotentials. The results given in Table 3.5 shows that there is little difference between the optical response coefficients using the two types of pseudopotentials. So we use norm-conserving pseudopotentials with the lower energy cut-off.

To summarize, we use norm-conserving, double-reference Kleinman-Bylander type pseudopotentials with nonlinear core corrections. The pseudopotentials have been extensively tested to reproduce the phaseshifts and atomic level spacings as the atomic potentials, give similar lattice constants and band structures as other LDA calculations, and give almost identical optical response coefficients as the better quality hardness-conserving pseudopotentials. With confidence in the pseudopotentials, we move on to the study of optical response in the wide gap semiconductors.

TABLE 3.5 Comparison of two types of pseudopotentials, norm-conserving and hardness-conserving pseudopotentials,[17] on the dielectric constants ε_∞ and the second-harmonic susceptibilities $d = \chi^{(2)}/2$ for zincblende SiC, BN, AlN, and GaN The norm-conserving pseudopotential is constructed with the normalization of the pseudo wavefunction inside the matching radius to be equal to that of the atomic wavefunction. The hardness-conserving pseudopotential is one type of norm-conserving pseudopotential which furthermore requires the hardness $\eta \equiv \partial\mu/\partial n = \partial^2 E/\partial n^2$ to be conserved in the pseudopotential construction; E is the energy, n is electron density, and μ is the chemical potential. The hardness-conserving pseudopotentials better describe charge transfer. The calculations with the two types of pseudopotentials give essentially identical results. The largest difference between two calculations is 1% in ε_∞ and 3% in d.

		E_{cut} (Hartree)	ε_∞	d_{xyz} (pm/V)
SiC	Norm-conserving	17	7.03	−12.45
	Hardness-conserving	40	7.03	−12.58
BN	Norm-conserving	25	4.56	2.80
	Hardness-conserving	45	4.58	2.83
AlN	Norm-conserving	25	4.59	0.01
	Hardness-conserving	45	4.56	−0.12
GaN	Norm-conserving	25	5.72	8.19
	Hardness-conserving	45	5.64	7.93

3.2 Four polytypes of Silicon Carbide

Calculations of optical response in four polytypes of SiC – 2H, 4H, 6H, and 3C – marks the beginning of our systematic studies on wide gap semiconductors.* Prior to this study, the scissors operators have been applied to small to medium gap semiconductors to produce excellent agreement with experiments in both the dielectric constants ε_∞ and the second-harmonic susceptibilities d.[4] Through the study of four polytypes of SiC, we find that using the scissors operator underestimates ε_∞ and d compared to experiment while LDA overestimates. Among the different SiC polytypes, trends are observed in the values and the local-field corrections to ε_∞ and d. Surprisingly, our calculations give a ratio $d_{xxz}/d_{zzz} = -1.5$ for 2H-SiC, different from the predictions of -0.5 from bond additivity, which is a basic assumption of semi-classical models of the second-harmonic susceptibilities.

3.2.1. Introduction

SiC is the only IV-IV compound known to form stable long-range ordered structures.[19] Over 200 polytypes have been observed among which the 6H polytype is predominant. One form of polytype, 3C, is cubic, exhibiting the zincblende structure (space group T_d^2-F$\bar{4}$3m). Another form, 2H, has the wurtzite structure (space group C_{6v}^4-P6_3mc). All other polytypes have either a hexagonal unit cell

* In Ref. 18, the pseudopotentials were constructed using the form suggested by Bachelet, Hamann, and Schlüter[5] and without nonlinear core corrections.[8] The results presented here are calculated using a different form of the pseudopotentials as specified in the previous section. We have also included the nonlinear local-field corrections for the second-harmonic susceptibilities in the current study. The results shown here are different from those presented in Ref. 18 by less than 5%.

(with $c/a > 2$) or a rhombohedral unit cell (space group C_{3v}^{5}-R3m).[20] In all polytypes, every atom is tetrahedrally surrounded by four atoms of the other species. The crystal structure may be regarded as a close packing of atoms of any one kind, say Si, with the other (C) atoms occupying half of the tetrahedral voids. The structure for 3C (zincblende) corresponds to the hexagonal close packing with a repeat unit of ABC. For 2H (wurtzite) the repeat unit is AB; for 4H ABCB; and for 6H ABCACB.

In all SiC polytypes, the chemical bonds between the Si and C atoms are the same. So it is an interesting problem to find how the packing order of the atomic layers alone can affect different physical properties, such as the dielectric constants ε_∞ and the second-harmonic susceptibilities $d = \chi^{(2)}/2$ which are currently studied. The experimental dielectric constants[19] show small changes from one SiC polytype to another, which are readily captured by our calculations. Semi-classical models, among which the bond-charge model[21] is the most successful, are useful in making order of magnitude estimates of second-harmonic susceptibilities, especially in a crystal with a single type of bond. All semi-classical models assume that the bonds contribute in an additive fashion, which constrains the ratios of the components of d (see Sec. 1.2).[22] Our calculations are not consistent with this picture. Our calculated d values disagree with a recent measurement on 6H-SiC but agree with one measurement on an unknown SiC polytype.[23] Our calculated values for 4H-SiC also lie close to the experiment on the unknown polytype.

In contrast to the small to medium gap semiconductors, we find that for wide gap semiconductors we have studied so far — diamond and 2H-, 4H-, 6H-, and 3C-SiC — the scissors operators needed to reproduce the experimental dielectric constants are less than the Δ needed to match the band gaps. This is also true for another wide gap material previously studied, namely urea.[1]

The linear response calculations are preparatory to the main goal of our present study, the calculation of the second-harmonic susceptibilities d for different SiC polytypes. In view of the linear response data, we decide our best guess for the second-harmonic susceptibility would be given by taking the self-energy correction Δ to be a parameter to be adjusted to the fit the dielectric constant ε_∞. In a previous study of an insulator, α-quartz, the use of Δ to match the static dielectric constant resulted in an excellent account of d_{xxx}.[24] We present three sets of results throughout the paper: LDA, band-gap-matching Δ_{gap}, and ε_∞-matching Δ_ε. The qualitative features of the calculation are not affected by the self-energy shift, only the calculated numerical values.

3.2.2. Results for Optical Response

Before studying SiC, we first calculate ε_∞ of diamond. Our LDA calculations for diamond — with and without local-field corrections — agreed with a previous calculation,[25] suggesting an overall reliability of our pseudopotential and other aspects of the calculation. However, we are surprised to find that adjusting the gap from the LDA value to the experimental one, using the scissors-operator approach (Δ=1.8 eV), failed to reproduce the experimental ε_∞ as shown in Table 3.6. This is in contrast to the work for a large class of small to medium gap semiconductors listed in the introduction. In diamond, we need increase the energy gap to only 84% of the experimental gap from the 77% given by the LDA. To deduce this, we apply a linear interpolation using the computed ε_∞ at Δ=0 and 0.5 eV. As a check on the linearity, we find that ε_∞ obtained with Δ=0.5 eV differs by less than 1% from the linear interpolation with Δ=0 and 1.8 eV. The value Δ=1.8 eV for diamond may be obtained by averaging Δ over the points Γ, X, and L from either of two GW calculations.[26,27] Another recent GW calculation[28] leads to a somewhat larger average Δ value (2.2 eV), which would only make the problem more extreme.

In wide-gap materials, for which until this paper we have only the example of urea,[1] there seem to be a "gap problem", that the effective gap to reproduce ε_∞ is less than the experimentally observed gap. (Although we have also studied α-quartz, the band gap is not well defined in this case.[30]) In the previous paragraph, we find this "gap problem" in diamond and we will see it for the SiC polytypes too. It may be generic in wide band gap materials.

As a first step to calculate the optical response of different polytypes of SiC, we studied the Δ dependence of ε_∞ and d in the case of 3C-SiC; we find that they are almost linear in Δ in the range studied, $0 \leq \Delta \leq 1.3$ eV. As shown in Figure 3.4, by linear interpolation using the computed values at Δ=0 and Δ=1.3 eV, we introduce an error of less than 1% for ε_∞ and less than 5% for d as compared to the computed values with different Δ. In the remainder of the paper, we will assume ε_∞ and d to depend linearly on Δ within the range $0 \leq \Delta < 1.3$ eV not only in 3C-SiC but also in the other three polytypes of SiC: 2H, 4H, and 6H.

Table 3.7 shows that the same Δ=0.75 eV reproduces the experimental values of the ordinary ε_o and extraordinary ε_e dielectric constants within 2% for all four SiC polytypes studied. In this Figure (3.4.a), the value of Δ corresponding to the experimental ε_∞ corresponds to 0.75 eV. The situation is almost the same in the other three polytypes 2H-, 4H-, and 6H-SiC. The best choice of Δ to match ε_∞ for

TABLE 3.6 Effects of the scissors operators on the dielectric constant of diamond. In contrast to the GW predictions[26,27] of $\Delta = 1.8$ eV, we find that $\Delta \approx 0.25$ eV reproduces the experimental dielectric constant. The E_{cut} we use is smaller than used in Ref. 25 because we use a softer pseudopotential.[10] However, the corresponding ε_∞ are essentially the same. The calculations done in Ref. 28 and Ref. 29 use Gaussian orbitals and orthogonalized-linear-combination-of-atomic-orbitals (OLCAO), respectively.

Self-energy correction Δ (eV)	E_{cut} (hartree)	No. of $\vec{k}$-points	ε_{00} (long wave)	ε_∞ (total)
0	17	60	5.96	5.77
0.25	17	60	5.75	5.66
1.8	17	60	5.27	5.11
0 (Ref. 25)	25	10	6.06	
0 (Ref. 25)	25	28	6.06	5.90
0 (Ref. 28)	Gaussian	10		5.5
0 (Ref. 29)	OLCAO	505		4.34
Exp. (Ref. 19)				5.67

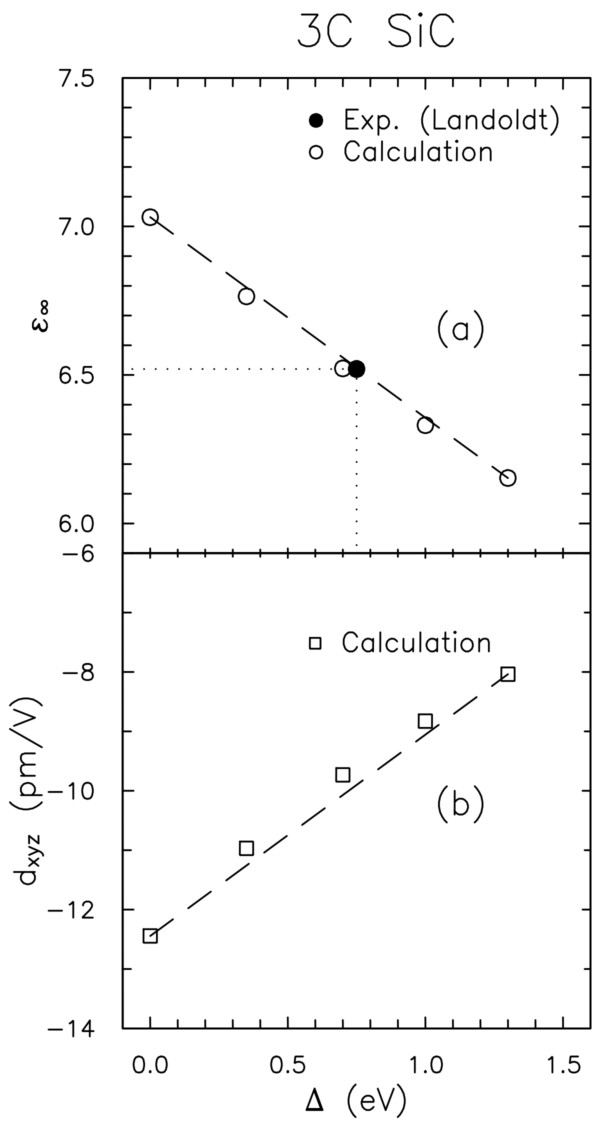

FIGURE 3.4 Dielectric constant ε_∞ and the second-harmonic susceptibility d_{xyz} of 3C-SiC versus the scissors shift Δ. The calculated values of ε_∞ and d, plotted with open symbols, are sublinear in Δ and lie close to the straight dashed line connecting the end points. Interpolating between the computed values with LDA (Δ = 0 eV) and the scissors shift which gives the correct band gap (Δ = 1.3 eV) yields an error, compared to the computed values, of less than 1% for ε and less than 5% for d. The experimental value for ε_∞ corresponds to Δ=0.75 eV, which is then used to predict d.

different polytypes range between 0.7 to 0.8 eV. We keep Δ=0.75 eV in all polytypes for simplicity. We continue to use 0.75 eV as Δ_ε, the self-energy correction to match ε_∞ for our calculations of the second-harmonic susceptibilities, too.

These results for the "gap problem" of SiC are in agreement with the work by Lambrecht *et al.*[31] They did experiments and LDA calculations on 3C- and 4H-SiC and found that the Δ needed to match the indirect band gaps are a few hundred meV greater than the Δ required to match the reflectivities. A recent study[28] of 3C-SiC (zincblende) gives the calculated ε_∞ of 6.7 with a LDA calculation using gaussian basis orbitals, compared to 6.95 for the present work.

To study the trends for nH-SiC polytypes, we use a special structural relation between 3C and ∞H-SiC to obtain the physical properties (e.g., ε_∞ and d) of ∞H-SiC from those of 3C-SiC. This structural relation between 3C and ∞H-SiC is easy to understand in the Hägg notation[20] which describes relations between successive Si-C bilayers. A passage from bilayers A$\rightarrow$B$\rightarrow$C$\rightarrow$A involves a translation of (1/3, 2/3) in the basal plane, whereas the passage from layers A$\rightarrow$C$\rightarrow$B$\rightarrow$A involves a translation of ($-1/3$, $-2/3$). Hägg denoted the former by "+" and the latter by "$-$". In the Hägg notation, 2H-SiC (AB$\cdots$) is represented by $+-\cdots$, 4H-SiC (ABCB$\cdots$) by $++--\cdots$, and 6H-SiC (ABCACB$\cdots$) by $+++---\cdots$. The 3C-SiC structure (ABC$\cdots$) is now represented by $+++\cdots$, or alternatively $---\cdots$ if we rotate the 3C-SiC crystal 180° along the z-axis (perpendicular to the Si-C planes). So if we cut the bulk 3C SiC crystal in half along the x-y plane and rotate the upper half by 180° along the z-axis, we will get the structure of $+++\cdots---\cdots$, which is equivalent to the structure of ∞H SiC. Since the boundary does not affect the bulk properties of the crystals, physical properties of

TABLE 3.7 Computed ordinary ε_o and extraordinary ε_e dielectric constants for four polytypes of SiC compared with experiment. The self-energy correction Δ_ε to reproduce (within 2% for all polytypes) the dielectric constant (also used in Table 3.9 to predict d) is about 65% the value needed to reproduce the indirect band gap Δ_{gap}. Results with $\Delta_\varepsilon = 0.75$ eV are obtained by linearly interpolating between LDA and Δ_{gap} values. The slight decrease in E_{cut} for 6H SiC is due to memory limitations on the Cray YMP.

	Method	2H	4H	6H	∞H (3C)
Δ_{gap} (eV)		1.2	1.1	1.0	1.3
No. $\vec{k}$ points		30	20	10	60
E_{cut} (eV)		17	17	16.5	17
ε_o	With Δ_{gap}	6.19	6.29	6.38	6.15
	LDA	7.00	7.05	7.09	7.03
	$\Delta_\varepsilon = 0.75$ eV	6.49	6.53	6.55	6.52
	Exp. (Ref. 19)	6.51	6.56	6.52	6.52
ε_e	With Δ_{gap}	6.46	6.51	6.57	6.15
	LDA	7.35	7.34	7.34	7.03
	$\Delta_\varepsilon = 0.75$ eV	6.79	6.77	6.76	6.52
	Exp. (Ref. 19)	6.84	6.78	6.68	6.52
$\varepsilon_e - \varepsilon_o$	With Δ_{gap}	0.27	0.22	0.19	
	LDA	0.35	0.29	0.25	
	$\Delta_\varepsilon = 0.75$ eV	0.30	0.24	0.21	
	Exp. (Ref. 19)	0.33	0.22	0.16	

∞H-SiC are directly related to those of 3C-SiC. In particular, the relations we use are

$$\begin{aligned} \varepsilon_o^{(\infty H)} &= \varepsilon_e^{(\infty H)} = \varepsilon^{(3C)}, \\ d_{zzz}^{(\infty H)} &= -2d_{xxz}^{(\infty H)} = 2d_{123}^{(3C)}/\sqrt{3}, \end{aligned} \tag{3.14}$$

as can be derived by transformation between cubic and hexagonal coordinates.[22]

Table 3.7 shows that the computed ε_∞ for nH-SiC with the same scissors operators Δ=0.75 eV capture the same trend as the experimental facts, namely ε_o, ε_e, and $\varepsilon_e - \varepsilon_o$ approach those of ∞H-SiC as n increases. In particular, ε_o remains more or less constant while ε_e and $\varepsilon_e - \varepsilon_o$ decrease with increasing n in nH-SiC. The trend is also true for the LDA calculations. We note here that E_{cut} for 6H-SiC is 0.5 hartree smaller than others (because of memory limits on the Cray YMP) and this might have caused the computed values of 6H-SiC to lie somewhat out of the trend. We also observed that using the band-gap-matching Δ, which means different Δ for different polytypes, does not produce the correct trend.

Table 3.8 shows that the second-harmonic susceptibilities d_{xxz} and d_{zzz} calculated for nH-SiC also follow the trend that with Δ=0.75 eV they approach those of ∞H-SiC as $n \to \infty$. Although the point group for crystals with C_{6v} symmetries including 2H, 4H, and 6H-SiC permits three independent tensor components, namely d_{xxz}, d_{zxx}, and d_{zzz}, Kleinman symmetry,[32] which is exact at zero frequency, implies $d_{xxz} = d_{zxx}$. The d we predict for all four SiC polytypes have the same order of magnitude as the experimental data on an unknown SiC polytype[23] and another experiment on 6H-SiC. With Δ=0.75 eV, the calculated d of 6H-SiC are within the the experimental uncertainty region of the unknown polytype. A recent experiment[33] on 6H-SiC gives larger values of d_{zzz} and smaller values of d_{xxz} compared to our calculations. Further experimental measurements and theoretical studies using other methods are needed to clarify this discrepancy. Table 3.8 also shows that d_{zzz} of 2H-SiC is unexpectedly small as compared with the other three polytypes. The trend for d in nH-SiC can be observed in Figure 3.5 in which we choose $1/n$ to be the x-axis. For both d_{xxz} and d_{zzz}, the variation is sublinear with $1/n$. The common end point value is somewhat below a linear fit to the small n calculations.

Bond-charge-model estimates,[21] shown in Table 3.8, of the second-harmonic susceptibilities for the SiC polytypes have the same order of magnitude as our calculated values. Because Si and C ions have the same ionic charge, the bond-charge model predictions for d are very sensitive to the choice of bond-charge and the ion radii as pointed out by Singh *et al.*[23] The bond-charge model and other semi-classical models* share tensorial addition of the single-bond second-order polarizability β, but differ as to how that β is defined. Hence the ratios of the macroscopic second-harmonic susceptibilities are independent of the semi-classical model chosen. This ratio is $d_{xxz}/d_{zzz}=-1/2$ for all nH SiC.[22] This is different from our calculations most manifestly in 2H-SiC for which we predict $d_{xxz}/d_{zzz} \approx -1.5$. In the bond-charge model, the d for *all* nH-SiC are the same, which is again in contrast to our predictions.

Figure 3.6 shows that the local-field corrections for both d_{xxz} and d_{zzz} for nH-SiC smoothly approach those for ∞H-SiC as n increases. As n increases the splitting in the local-field decreases monotonically to the degenerate $n = \infty$ case. The local-field corrections are one order of magnitude smaller than the long-wave contribution. Our calculations show that the local-field corrections to ε_o and ε_e are

* For a list of the semi-classical models, see Ref. 21.

TABLE 3.8 Computed static second-order nonlinear susceptibilities $d = \chi^{(2)}/2$ (pm/V) for 4 polytypes of SiC. Values for ∞H-SiC are obtained from 3C-SiC results by $d_{zzz}^{(\infty H)} = -2d_{xxz}^{(\infty H)} = 2d_{xyz}^{(3C)}/\sqrt{3}$.[22] The values of Δ_{gap} are given in Table 3.7. Experiment 1 is on 6H-SiC with the relative signs of d_{xxz} and d_{zzz} determined but with the absolute signs of d undetermined. Experiment 2 is done on an unknown SiC polytype,[23] By using a Miller's rule,[34] namely, $d_{ijk}(0)/[\chi_{ii}(0)\chi_{jj}(0)\chi_{kk}(0)] = d_{ijk}(\omega)/[\chi_{ii}(2\omega)\chi_{jj}(\omega)\chi_{kk}(\omega)]$, the static limits of both experiments are obtained. The bond-charge model predicts the same d for all SiC polytypes.

	With Δ_{gap}		LDA		Interpolation Δ_ε =0.75 eV	
	d_{xxz}	d_{zzz}	d_{xxz}	d_{zzz}	d_{xxz}	d_{zzz}
2H-SiC	4.4	−3.1	6.6	−4.7	5.2	−3.7
4H-SiC	5.0	−7.9	7.5	−11.8	5.8	−9.1
6H-SiC	5.3	−9.7	7.7	−14.3	5.9	−10.9
∞H-SiC	4.6	−9.2	7.2	−14.4	5.7	−11.4
Exp.1 ($\lambda = \infty$)					$\pm$2.2	$\mp$22
Exp.1 ($\lambda = 1.06\mu$m) (Ref. 33)					$\pm$2.5	$\mp$25
Exp.2 ($\lambda = \infty$)					6.9$\pm$0.8	−11.6$\pm$1.3
Exp.2 ($\lambda = 1.06\mu$m) (Ref. 23)					7.9$\pm$0.9	−13.5$\pm$1.5
Bond-charge model (Ref. 21)					4	−8

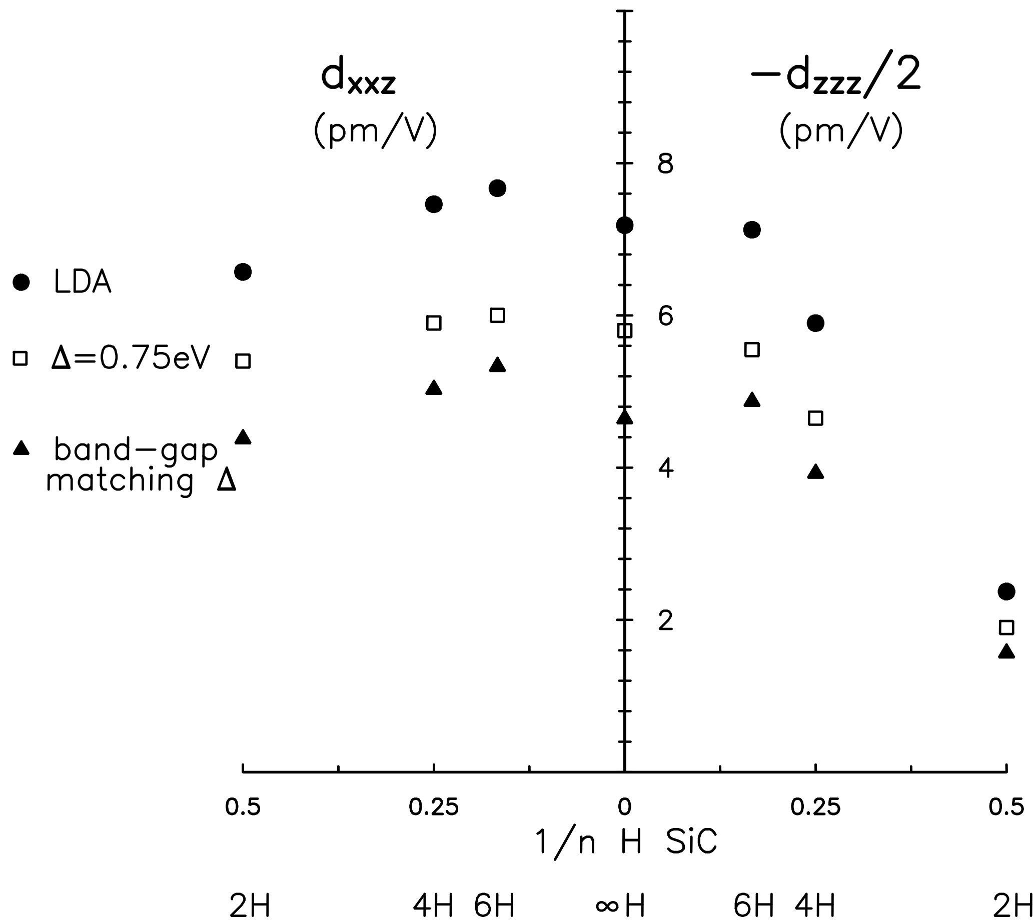

FIGURE 3.5 The trend of d_{xxz} and d_{zzz} in nH-SiC for different scissors shift Δ. We plotted $-d_{zzz}/2$ to combine the two d components in one figure. In ∞H-SiC, the two d components are related by $d_{zzz}^{(\infty H)} = -2d_{xxz}^{(\infty H)} = 2/\sqrt{3}d_{xyz}^{(3C)}$. Our calculated values are given by the solid symbols, ● for LDA and ▲ for scissors shifts that reproduces the band gaps. Linearly interpolating between the two calculated values with Δ=0.75 eV gives □ in the figure.

also small. For the four polytypes considered, they all lie between −3.5% and −4%.

Our calculations are also converged in the special $\vec{k}$-point summation for all the SiC polytypes. In 3C-SiC, we use 60 $\vec{k}$-points in the irreducible Brillouin zone, in 2H 30, in 4H 20, and in 6H 10. For the hexagonal structures, the $\vec{k}$-points use belong to Group IV discussed in Appendix A. Convergence studies are carried out on 2H-SiC which has the smallest unit cell among the hexagonal structures. In 2H-SiC, varying the number of integration points in the plane from 6 to 10, with two layers, leads to a variation in the two components of ε_∞ and d by no more than 0.4% and 1% respectively. Variation of the number of planes from 2 to 3 (with 6 integration points per plane) leads to corresponding variations of no more than 1% and 3% respectively. Based on past experience with the sum rules,[35] these results imply that the d calculations are converged to 5%, and that the ε_∞ values are converged to within 2%. In 4H and 6H, the unit cells are 2 and 3 times as long as in 2H, and hence the Brillouin zones are 1/2 and 1/3 as high. Using 2 and 1 layer of $\vec{k}$-points for 4H and 6H in the z-direction gives larger and equal $\vec{k}$-point density, respectively, as the 3-layer calculation for 2H.

3.2.3. Summary for the SiC calculations

We calculate dielectric constants ε_∞ and second-harmonic susceptibilities d for four polytypes of SiC in addition to ε_∞ for diamond. We use the LDA as well as the LDA with a self-energy correction in the form of a scissors operator.[35] The LDA overestimates the experimental values of ε_∞ by 2% in diamond and about 7% in the SiC polytypes. In all the wide band gap materials we have studied so far (urea,[1]

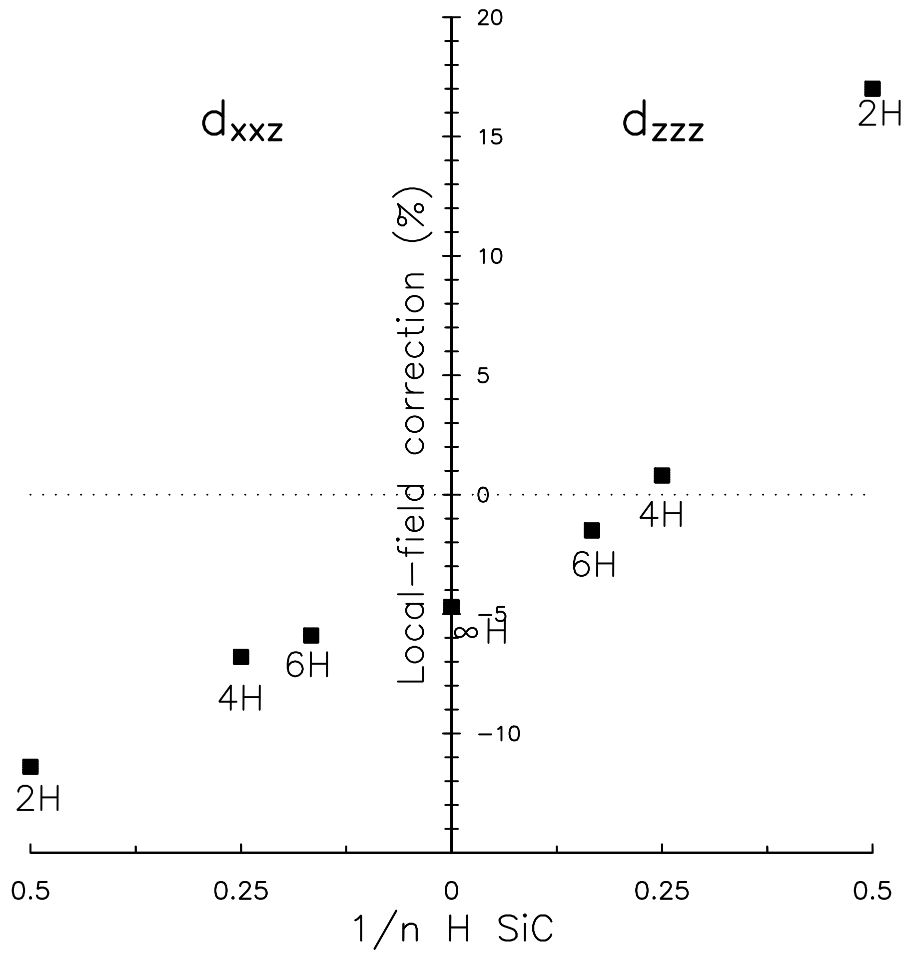

FIGURE 3.6 Local-field corrections to second-harmonic susceptibilities d_{xxz} and d_{zzz} of nH-SiC with self-energy correction $\Delta = 0.75$ eV. We observe two facts: (1) All local-fields corrections are within 20% of the total contribution. (2) The local-field form a trend among the polytypes. In the case of ∞H-SiC, $d_{xxz} = -d_{zzz}/2$ by symmetry. So the local-field corrections are identical. With LDA and band-gap-matching Δ, the local-field corrections are very similar to the present case.

diamond, and four polytypes of SiC) we observe the curious fact that the Δ needed to reproduce the dielectric constants is less than that needed to reproduce the band gap. We find in particular that with Δ=0.75 eV for all four SiC polytypes, we can reproduce the experimental ε_∞ within 2%. We further find that with the same Δ=0.75 eV, the calculated d_{xxz} and d_{zzz} for nH-SiC with $n \geq 4$ are all close to the values of an experimental measurement on an unknown SiC polytype. A recent experiment on 6H-SiC gives different values of d_{zzz} larger than our calculated values and d_{xxz} smaller. This experiment gives the ratio of $d_{xxz}/d_{zzz} = -0.1$ which is qualitatively different from our calculated ratio -0.54.

In the calculations of d, we find that d_{zzz} of 2H-SiC (wurtzite) is unexpectedly small as compared to the other three polytypes. The results are not consistent with a bond-charge model in which the hyperpolarizability is a tensorial sum of bond hyperpolarizabilities.[22] This is a surprise for this σ-bonded system.

The local-field corrections to the SiC polytypes are about 6% for ε_∞ and -12% to +18% for the second-harmonic susceptibilities d. For nH-SiC, both the values and the local-field corrections to d form a trend among the polytypes.

3.3 III-V nitrides

The III-V nitrides – BN, AlN, GaN, and InN – are another series of wide band gap semiconductors. Through the study of three of them, BN, AlN, and GaN, we can gain further understanding of the effect of scissors operators on optical coefficients in wide gap materials. These compounds exhibit both zincblende and wurtzite structures which allows us to test the validity of bond-additivity.

3.3.1 Introduction

The III-nitride compounds have recently attracted extensive experimental[16] and theoretical[36,37,38,39] interest. Their physical properties such as a wide band gap, low compressibility, and high thermal conductivity make them promising candidates for short-wavelength (green, blue, and ultraviolet) electroluminescent devices and high-temperature diodes and transistors.[16] Blue and green light emitting diodes based on the nitrides have already surpassed the traditional SiC and ZnSe diodes in brightness and lifetime.[40] At the beginning of this year, the first multi-quantum well structure InGaN blue laser was successfully fabricated.[41] Figure 3.7 shows that the band gaps for the III-V nitrides range from 2 eV in InN to 11 eV in BN. The lattice constant mismatch between AlN and GaN is only 3%, making it easy to grow AlN-GaN mixtures. With these nitrides and their mixtures, one can cover the blue to ultraviolet region in luminescent devices which are unaccessible with Si or GaAlAs based materials.

There have been recent efforts on measuring the second-harmonic susceptibilities on AlN and GaN for their potential use as frequency-doubling and electrooptical devices.[42,43] Theoretical efforts have been mainly directed towards structural properties,[36] band structures,[37,38,39,44] and linear optical properties.[39,44] The current study provides reliable theoretical estimates of the second-harmonic susceptibility for three of the compounds: BN, AlN, and GaN. Our calculations show that the d of all three compounds are a few pm/V, comparable to those of ADP and KDP.

Bond-additivity is often used to relate the different components of the second-

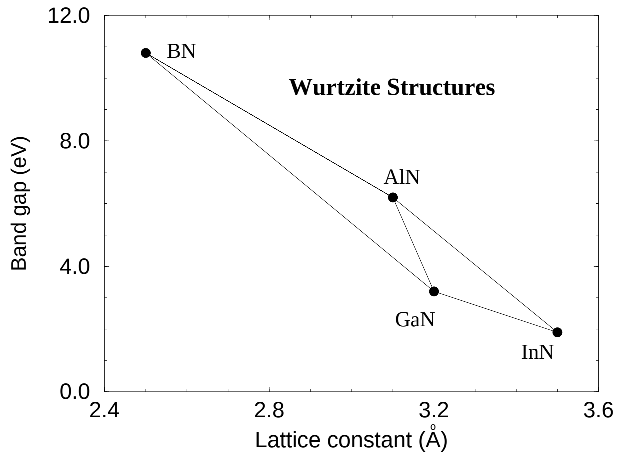

FIGURE 3.7 Band gap versus in-plane lattice constant of the III-V nitrides in the wurtzite structure. The region bounded by solid lines give the band gaps of the possible mixtures of the compounds.

harmonic susceptibilities d. We have seen from the SiC calculations that bond-additivity works in 4H- and 6H-SiC but fails in 2H-SiC. We continue to test bond-additivity in the III-V nitrides.

The eigenvalue of the 3d electrons in Ga atom is -21.7 eV, very close to the eigenvalue of the 2s electrons in N atom which is -18.7 eV. In the GaN compound, the Ga-3d and N-2s electrons hybridize (see the band structure plot in Table 3.12). We carry out two independent calculations with the Ga-3d electrons in the core and in the valence. We find that the error in freezing the Ga-3d electrons in the core is 7% in ε_∞ and 25% in d.

We exclude InN from our current study for three reasons: (1) the In-4d electrons hybridize with the N-2s and need be take into account in a larger calculation with the In-4d electrons in the valence, (2) the LDA calculated conduction band energy at Γ-point lies at about 0.1 eV *below* the valence band edge and thus makes the calculations difficult to converge, and (3) In is a heavy element in which spin-orbit coupling may be important. Investigation of the spin-orbit coupling given in Appendix B shows that the splitting of the valence bands is rather small, 0.021 eV, but the splitting in the conduction bands is large, 0.795 eV. Ignoring spin-orbit coupling may introduce an error of a few percent.

Our previous studies on urea, diamond, and four polytypes of SiC suggest that using scissors operators underestimate optical response coefficients in wide gap semiconductors. The III-V nitrides provides an opportunity to further understand the effects of scissors operators in wide gap materials.

3.3.2 Calculated resuts

In this subsection, we first present the calculated dielectric constants ε_∞ and second-harmonic susceptibilities d for BN, AlN, and GaN. Next, we test the validity of bond-additivity for these materials. This is followed by the investigation of the role of the Ga-3d electrons in GaN. Finally, we provide some details on the convergence study.

Dielectric constants ε_∞. Table 3.9 shows that our dielectric constants ε_∞ calculated using LDA are in reasonable agreement with available experiment. Experimental data are scarce and may suffer from poor samples. Comparison with other calculations[39,44,45] are also listed in Table 3.9. For GaN our ε_∞ agrees with a full-potential linear-muffin-tin-orbital calculation.[44] Our calculation is the only one which includes local-field corrections. Our calculations using scissors operators reduce ε_∞ by about 15% compared to our LDA calculations and make ε_∞ smaller than experimental values. Our choice of the scissors shifts are: BN 2.5 eV, AlN 2.0 eV, and GaN 1.5 eV. The scissors shifts are obtained by comparing our LDA band structures with the quasiparticle band structures from the GW calculations. Details of the comparison can be found in Table 3.4. In these wide gap materials, we continue to observe that the scissors operators give smaller values for ε_∞.

Second-harmonic susceptibility d. Table 3.10 gives the calculated results for d of BN, AlN, and GaN: in wurtzite, $d^{(w)}_{xxz}$ and $d^{(w)}_{zzz}$; in zincblende, $d^{(z)}_{xyz}$. For wurtzite GaN, the measurement of Miragliotta *et al.*[51] is consistent with our predictions using LDA except for the reported overall sign. However, this overall sign was not determined experimentally relative to the atomic co-ordinates,[52] so there is no disagreement. For AlN we note two interesting points: (i) $d^{(z)}_{xyz}$ and $d^{(w)}_{xxz}$ almost vanish; (ii) $d^{(w)}_{zzz}$ is negative while $d^{(w)}_{zzz}$ for BN and GaN are positive. The only experiment[50] on single-crystal wurtzite AlN shows that $d^{(w)}_{xxz}$ is almost zero and that $d^{(w)}_{zzz}$ is negative, in agreement with our calculations. One experiment[42] on polycrystalline wurtzite AlN gives $|d^{(w)}_{zzz}| = 1.0$ pm/V, about 1/4 of our predictions. We believe, as suggested in Ref. 42, that this lower $d^{(w)}_{zzz}$ is caused by incomplete alignment of crystallites along the z-axis. Another experiment[43] on polycrystalline wurtzite AlN reports $d^{(w)}_{zzz}/d^{(w)}_{xxz} = 3$. But it is unclear how this ratio from poly-crystallites is related to that of the single crystal without the knowledge of the orientation distribution of the crystallites. In comparison with the bond-charge model estimations, our calculated d are four times smaller. Table 3.10 also shows that the scissors operators give underestimations for d.

Tests of bond-additivity. Using our calculated LDA values of the second-harmonic susceptibilities, we test the validity of bond-additivity in the III-V nitrides. As al-

TABLE 3.9 Dielectric constants ε_∞ for BN, AlN, and GaN. Our calculated dielectric constants are generally consistent with limited experimental data. The superscripts refer to the ordinary and extraordinary components, respectively. Results from other LDA calculations include two independent linear-muffin-tin-orbital (LMTO) calculations, one with atomic sphere approximation (ASA) and the other with full potential (FP). Only the present calculation includes local-field corrections. The calculations using scissors operators give small values than experiment. The scissors shifts used are taken from Table 3.4: BN 2.5 eV, AlN 2.0 eV, and GaN 1.5 eV.

		Zincblende	Wurtzite	
		ε_∞	$\varepsilon_\infty^{(o)}$	$\varepsilon_\infty^{(e)}$
BN	LMTO-ASA (Ref. 39)	4.14	4.19	4.06
	Present (LDA)	4.56	4.51	4.69
	Present (scissors)	3.99	3.95	4.08
	Exp. (Ref. 46)	4.5		
AlN	LMTO-ASA (Ref. 39)	3.90	3.91	3.77
	Present (LDA)	4.61	4.42	4.70
	Present (scissors)	3.93	3.78	3.94
	Exp. (Ref. 47)		4.84	
	Exp. (Ref. 48)		4.68	
GaN	LMTO-ASA (Ref. 39)	4.78	4.71	4.62
	LMTO-FP (Ref. 44)	5.96	5.48	5.65
	Present (LDA)	5.74	5.54	5.66
	Present (scissors)	4.87	4.75	4.85
	Exp. (Ref. 49)		5.35±0.20	$\varepsilon_\infty^{(o)} \pm 4\%$

TABLE 3.10 Second-harmonic susceptibilities d of three III-nitride materials. Our calculations closely agree with experiments on wurtzite AlN and GaN. The magnitudes of d from our calculations are four times smaller than the bond-charge model estimates. The experimental data for AlN is corrected by using a new reference for d of quartz. All the experimental values for d are our extrapolation to ω=0 using Miller's rule. The superscript (z) and (w) refer to zincblende (cubic) and wurtzite (hexagonal), respectively. See text for discussions of additional experimental results for AlN. The scissors shifts are the same as in Table 3.9.

		Zincblende	Wurtzite	
		$d^{(z)}_{xyz}$	$d^{(w)}_{xxz}$	$d^{(w)}_{zzz}$
BN	Present (LDA)	2.65	-1.37	2.66
	Present (scissors)	1.70	-0.88	1.72
AlN	Present (LDA)	-0.01	-0.12	-4.12
	Present (scissors)	0.00	-0.05	-2.31
	Bond-charge model			-17
	Exp. (Ref. 50)		$\leq \|0.26\|$	-6.3 ± 3.5
GaN	Present (LDA)	8.19	-3.23	5.36
	Present (scissors)	5.05	-2.13	3.46
	Bond-charge model			-26
	Exp. (Ref. 51)		2.66	-5.35

ready discussed Sec. 1.2, assuming that the bonds in both the zincblende and the wurtzite structures of each compound are the same, the bond-additivity predicts a simple relation between the different components of d,

$$d^{(w)}_{zzz} = -2d^{(w)}_{xxz} = 2/\sqrt{3}d^{(z)}_{xyz}. \tag{3.15}$$

Figure 3.8 compares the computed and available experimental scaled susceptibilities in Eq. (3.15). If bond-additivity held, the scaled values of d should collapse to a single point for each compound. Based on our calculations, this is true for BN, but begins to break down for GaN where $2/\sqrt{3}d^{(z)}_{xyz}$ is almost double the value of $d^{(w)}_{zzz}$. The most severe violation of Eq. (3.15) occurs in AlN, where the computed $d^{(w)}_{zzz}$ is -4.1 pm/V but $d^{(w)}_{xxz}$ and $d^{(z)}_{xyz}$ are almost zero. From the experiment[50] on single crystal of AlN, the ratio of $d^{(w)}_{xxz}/d^{(w)}_{zzz}$ is less than 0.04 compared to our computed ratio of 0.03.

In the experimental paper reporting the measurement of d in AlN, the authors speculated that the lattice distortion in wurtzite AlN, which is 2% from perfect tetrahedral coordination, might make the bonds inequivalent which could lead to a small ratio of $d^{(w)}_{xxz}/d^{(w)}_{zzz}$. To test this possibility, we repeat the calculation using the perfect tetrahedral geometry while preserving the unit cell volume. The results in Table 3.11 show that a 2% variation in the lattice structure yields a 20% change in $d^{(w)}_{zzz}$. However, $d^{(w)}_{xxz}$ remains to be small and the ratio of $d^{(w)}_{xxz}/d^{(w)}_{zzz} = 0.1$ for the perfect tetrahedral geometry is still qualitatively different from the bond-additivity prediction of -0.5. So we rule out the possibility that the vanishingly small ratio of $d^{(w)}_{xxz}/d^{(w)}_{zzz}$ is the result of the lattice distortion.

The Ga-3d electrons. In GaN, the Ga-3d electrons lie very close to the energy of the N-2s electrons (see the band structure plot in Table 3.11). To take into

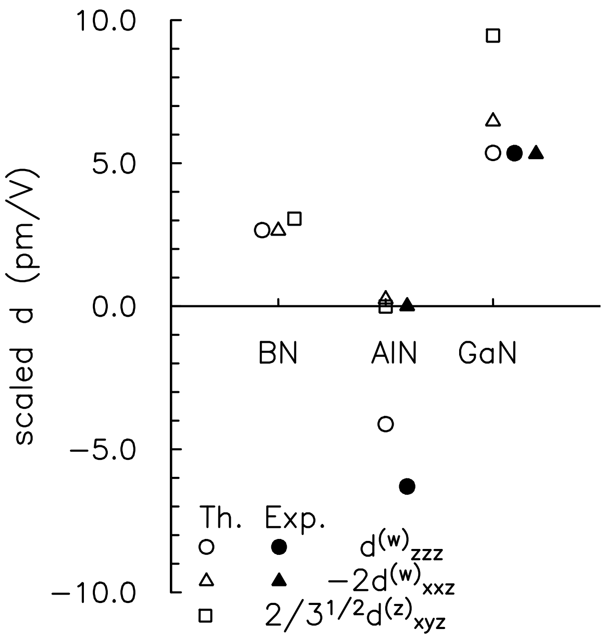

FIGURE 3.8 Rescaled second-harmonic susceptibilities, $d^{(w)}_{zzz}$, $-2d^{(w)}_{xxz}$, and $2/\sqrt{3}d^{(z)}_{xyz}$, for BN, AlN, and GaN in zincblende (z) and wurtzite (w) structures. If bond-additivity held, that the macroscopic susceptibilities d are a tensorial sum of the microscopic susceptibilities of the individual bonds, the rescaled d should collapse to a single point for each material. This is not the case for AlN or GaN. The hollow symbols report our LDA calculations and the solid symbols experiment.

account the hybridization between the Ga-3d and N-2s electrons, one needs to include the Ga-3d electrons in the valence band instead of freezing them in the core. Describing the Ga-3d electrons using pseudopotentials requires a much higher energy cut-off at 50 hartree. In the calculations given in Tables 3.9 and 3.10, the Ga-3d are treated as core electrons. To investigate the effects of the Ga-3d, we carry out another calculation on zincblende GaN by including the Ga-3d in the valence band. Table 3.11 summarizes the difference between the two calculations on four

TABLE 3.11 Geometry dependence of the ratio $d^{(w)}_{xxz}/d^{(w)}_{zzz}$ in wurtzite AlN. The experimental geometry is distorted from the perfect tetrahedron by 2%. We carry out two separate calculations one with the experimental geometry and the other with perfect tetrahedral geometry with the same volume of the unit cell. The calculated $d^{(w)}_{zzz}$ differ by about 20%. However, the ratio $d^{(w)}_{xxz}/d^{(w)}_{zzz}$ for the perfect tetrahedron remains much too small compared to the bond-additivity predictions of -0.5.

	Exp. geometry	Perfect tetrahedron
c/a	1.601	1.633
u/c	0.382	0.375
$d^{(w)}_{xxz}$ (pm/V)	-0.12	-0.20
$d^{(w)}_{zzz}$ (pm/V)	-4.12	-3.28
$d^{(w)}_{xxz}/d^{(w)}_{zzz}$	0.03	0.06

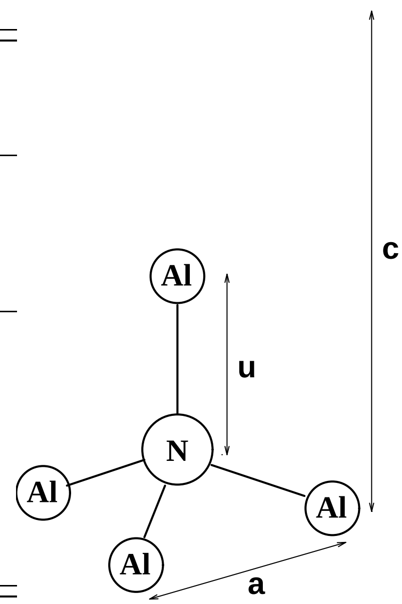

properties: (1) the LDA determined lattice constant, (2) LDA band structures, (3) the dielectric constant ε_∞, and (4) the second-harmonic susceptibility $d^{(z)}_{xyz}$. With the Ga-3d electrons in the valence, the LDA lattice constant is 0.6% smaller than the experimental value of 8.54 bohr, a 2% improvement from freezing the Ga-3d in the core. The band structure differ by 0.4 eV at different $\vec{k}$-points but the averaged gap over Γ, X, and L differ by less than 0.1 eV. The largest change is in the LDA value for $d^{(z)}_{xyz}$ which is *decreased* by 25% with the inclusion of the Ga-3d in the valence band. In contrast, the dielectric constant ε_∞ *increased* by 7%. We have not carried out a similar calculation for wurtzite GaN because of the memory limits on the CRAY-YMP.

Convergence. Sufficient convergence is reached for our calculations. The only two convergence parameters for our method are the energy cut-off for the plane-waves (E_{cut}) and the number of $\vec{k}$-points to sample the integration. Using E_{cut}=25 hartree in zincblende BN we find that the eigenvalues for the lowest 50 bands have converged to about 0.1 eV compared to using $E_{cut} = 50$ hartree. The choice of E_{cut} depends on the pseudopotentials. Since the $2p$ pseudopotential of N is deepest, we use $E_{cut} = 25$ hartree for all the calculations. We also converge our calculations by increasing the number of $\vec{k}$-points. In the zincblende structures, we use 60 $\vec{k}$-points[53] in the irreducible Brillouin zone. In the wurtzite structure, we use 3 z-direction layers with 10 Group IV $\vec{k}$-points (see Appendix A) on each layer in the irreducible Brillouin zone. The sum rules[4] associated with ε_∞ and d are used to test the convergence. With the above choices for E_{cut} and the number of $\vec{k}$-points, the sum rules are all satisfied within 2%. Decreasing the number of $\vec{k}$-points by half change the dielectric constants by at most 1% and the second-harmonic susceptibilities by at most 5%.

3.3.3 Summary

In summary we provide calculations using LDA and scissors operators for the dielectric constant ε_∞ and the second-harmonic susceptibilities d of BN, AlN and GaN in zincblende as well as wurtzite structures. Our LDA calculations of ε_∞ agree with available experiments. In wurtzite AlN and GaN, our calculated LDA values

TABLE 3.12 Influence of the Ga-3d electrons in GaN zincblende calculations. The band structure plot is produced by a full-potential linear-augmented-plane-wave calculation. At the bottom of the plot, the Ga-3d electrons hybridize with the N-2s electrons. The table lists plane-wave pseudopotential calculations with the Ga-3d electrons in the core and in the valence. The LDA determined lattice constant a_{LDA} (in unit bohr) are smaller than the experimental value of 8.54 bohr by 2.5% and 0.6% for the 3d-core and 3d-valence calculations, respectively. The band structures (in unit eV) differ by ± 0.4 eV at different $\vec{k}$-points along the edges of the valence (v) and conduction (c) bands. The averaged direct gap, however, differ by less than 0.1 eV. The 3d-valence calculations give a 7% increase in the dielectric constant ε_∞. For the second-harmonic susceptibility $d^{(z)}_{xyz}$, including the Ga-3d electrons in the valence decreases $d^{(z)}_{xyz}$ by 25% in the LDA calculation and 12% in the scissors calculation. Both calculations – 3d-core and 3d-valence – use 1.5 eV as the scissors shift and 28 $\vec{k}$-point to sample the integration . The energy cut-off are 25 hartree and 50 hartree for the 3d-core and 3d-valence calculations, respectively.

		3d-core	3d-valence
a_{LDA}	(bohr)	8.33	8.49
LDA	Γ_c	1.93	1.55
band	X_v	−2.40	−2.7
structure	X_c	3.25	3.23
	L_v	−0.82	−1.00
	L_c	4.69	4.36
ε_∞	LDA	5.72	6.16
	Scissors	4.87	5.21
$d^{(z)}_{xyz}$	LDA	8.19	6.14
(pm/V)	Scissors	5.05	4.42

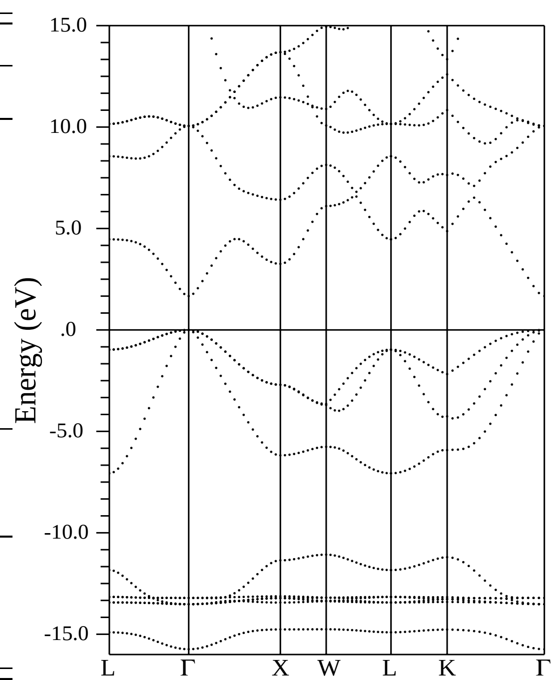

of d agree with the single-crystal measurements.

We find that the bond-additivity picture fails to explain the ratios $d^{(z)}_{xyz}/d^{(w)}_{zzz}$ and $d^{(w)}_{xxz}/d^{(w)}_{zzz}$ in AlN and $d^{(z)}_{xyz}/d^{(w)}_{zzz}$ in GaN. By calculating d on a perfect tetrahedrally coordinated structure, we rule out the the possibility[50] that the lattice distortion in wurtzite AlN causes the small measured ratio of $d^{(w)}_{xxz}/d^{(w)}_{zzz}$. Experimental measurement of $d^{(z)}_{xyz}$ in zincblende AlN will stringently test our predictions of a vanishingly small value.

The Ga-3d electrons hybridize with the N-2s electrons in GaN. Comparing two calculations with the Ga-3d in the valence and in the core shows that freezing the Ga-3d in the core leads to (1) 2% error in LDA lattice constant, (2) 0.4 eV error in the band structure, (3) 7% error in ε_∞, and (4) 25% error in d.

In the III-V nitrides, the scissors operators underestimate the dielectric constant ε_∞ and the second-harmonic susceptibility d. This is consistent with our previous studies on other wide gap materials including urea,[1] diamond, and four polytypes of SiC.[18] The underestimation of the optical coefficients using scissors operators may be generic in all wide gap materials.

3.4 Local-field corrections to second-harmonic susceptibility

In this section, we discuss the local-field corrections to the second-harmonic susceptibility. In Chapter 2, we showed that there are three orders of local-field corrections coming from the linear and nonlinear local fields. The size of the three order of local-field corrections is discussed first followed by the relation between the linear and nonlinear local fields.

Relative size of the three orders of local-field corrections. There are two types of local-field corrections to the second-harmonic susceptibility, the linear and the nonlinear local fields arising from the linearly and nonlinearly induced densities, respectively. As shown in Sec. 2.6, the nonlinear local-field correction is algebraically related to that of the linear local-field correction. The combined total local-field consists of three orders of corrections involving one, two, three matrix elements of the linear local field [cf. Eq. (2.46)]. In Figure 3.9, we plot the relative local-field corrections from the three different orders on a log scale versus different materials. A clear hierarchical structure is observed: the relative size of the correction decreases by roughly an order of magnitude with each increasing order of the local field. The leading correction comes from the first-order local-field and gives a 10–20% decrease in most cases. The second- and third-order local-field corrections are around 1% and 0.1%, respectively. Figure 3.9 indicates that neglecting the second- and third-order local-field corrections leads to an error of at most a few percent. In 4H-SiC, the first-order correction happens to be small because of the accidental cancellation between the ccv and the vvc terms. Similarly, for Se, the ccv and vvc terms of the second-order corrections almost cancel thus leading to a rather small second-order local-field correction. Among the materials studied, AlP, AlAs, GaP, GaAs, and 3C-SiC have zincblende structure; Se has trigonal structure, and 2H- (wurtzite), 4H-, and 6H-SiC have hexagonal symmetry. The III-V nitrides BN, AlN, and GaN exhibit both zincblende and wurtzite structures of which only the d_{zzz} component of the wurtzite result is shown in Figure 3.9. The other component d_{xxz} of the wurtzite structure and d_{xyz} of the zincblende structure give similar conclusions.

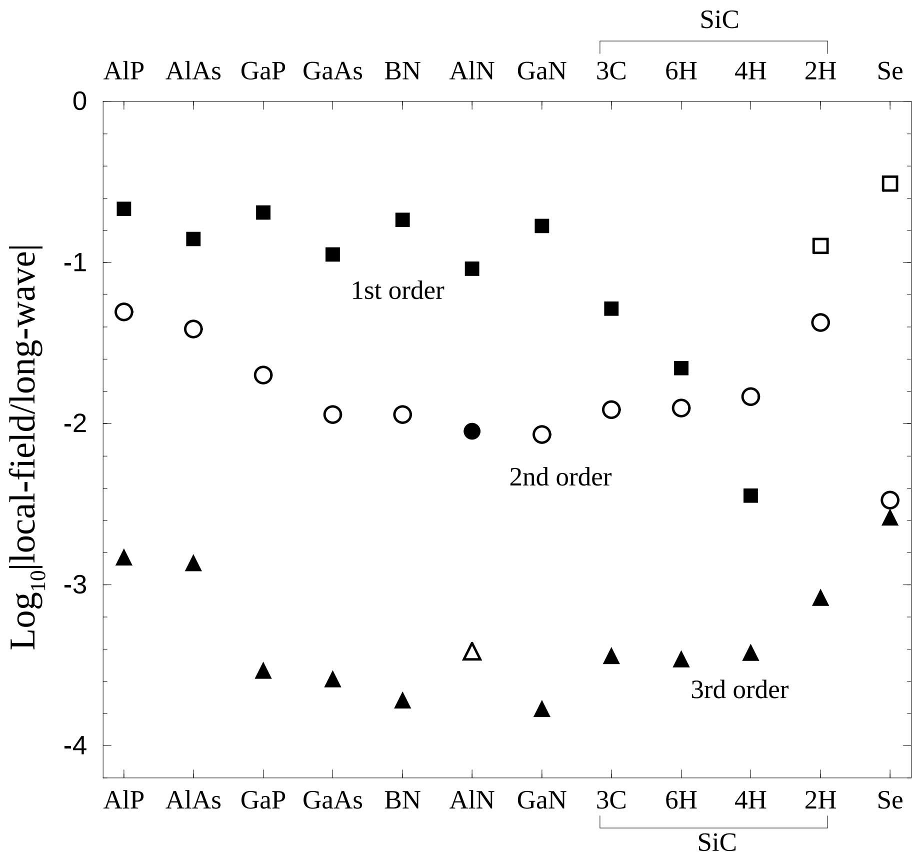

FIGURE 3.9 Local-field corrections to the second-harmonic susceptibility for different semiconductors. For each material is plotted three different contributions containing the first-, second-, and third-order local-field corrections, respectively. The first-, second-, and third-order local-field corrections are indicated by (□, ■), (○,●), and (△, ▲), respectively. The filled and hollow symbols correspond to + and − signs of the relative local-field corrections, respectively. The dominant correction comes from the first-order local field with each successive order about an order of magnitude smaller. Ignoring local-field corrections of second- and third-orders reduces computing time by half while producing errors of a few percent or less.

TABLE 3.13 The numerical ratio of the corrections from the nonlinear ($\phi^{(2)}$) and linear ($\phi^{(1)}$) local fields to the second-harmonic susceptibility for zincblende semiconductors. In the static limit, which is used for the current calculation, the ratio should be 1/2 as shown in Eq. (1.41). The agreement between the numerical ratio and the factor of 1/2 indicates that the calculations are converged to a few percent or better.

	AlP	AlAs	GaP	GaAs	BN	AlN	GaN	3C-SiC
$\dfrac{\text{1st correction from } \phi^{(2)}}{\text{1st correction from } \phi^{(1)}}$	0.50	0.50	0.48	0.48	0.50	0.50	0.50	0.50

Relation between the linear and nonlinear local-field corrections. The leading local-field correction to the second-harmonic susceptibility contains contributions from both the linear ($\phi^{(1)}$) and nonlinear ($\phi^{(2)}$) local fields. We have shown in Sec. 2.6 that, in the static limit, the first-order nonlinear local-field correction is mathematically equal to half the first-order linear local-field correction. Achieving the factor of a half numerically is nontrivial because it requires a sum over a complete set of states and the integration over the Brillouin zone. We can use this nontriviality to give an independent check on the numerical convergence of our calculation – the completeness of the basis functions and the accuracy of the integration – by separately evaluating the linear and nonlinear local-field corrections. As shown in Table 3.13, the numerical ratios are very close to 1/2 indicating that our calculations have converged to within a few percent.

In this section, we have shown that among the three orders of local-field corrections to the second-harmonic susceptibilities, the first-order correction gives the dominant contribution. The second- and third-order corrections are one and two orders of magnitude smaller than the first-order correction, respectively. We have also demonstrated numerically that the nonlinear local field correction is equal to half the linear local-field correction. Among the materials studied, the total local-field correction ranges from -21% to $+30\%$. The local-field corrections have to be included to obtain quantitative agreement with experiment.

3.5 Conclusions

We carefully construct and test the pseudopotentials before engaging in the optical response calculations. We use Troullier-Martins' type norm-conserving pseudopotentials with two-reference Kleinman-Bylander projection operators and nonlinear core corrections. The pseudopotentials are tested to give good phaseshifts and atomic levels splittings as the atomic potentials. With our choice of the pseudopotentials, the calculated LDA lattice constants, band structures, and optical response coefficients agree with full-potential linear augmented plane-wave calculations and the better-quality hardness-conserving pseudopotentials. In GaN where the Ga-3d levels hybridize with the N-2s level, including the Ga-3d in the valence in the zincblende structure yields a 7% increase in the dielectric constant and a 25% decrease in the second-harmonic susceptibility compared to treating the Ga-3d in the core. We expect similar changes to the wurtzite structure of GaN.

From the study of diamond, four polytypes of SiC (3C, 2H, 4H, and 6H), BN, AlN, and GaN, we find that for wide band gap semiconductors, the scissors operators give optical response coefficients – the dielectric constants and the second-harmonic susceptibilities – too small compared to experiment. An earlier study[1] of another wide gap material, urea, gives the same conclusion. This is in direct contrast to the small to medium band gap semiconductors where the scissors operators give optical response coefficients in excellent agreement with experiment. In the wide band gap materials, the experimental measurements for the dielectric constants lie between our scissors and LDA calculation. Our calculated second-harmonic susceptibilities using LDA on SiC, AlN, and GaN are in fair agreement with experimental results. However, a recent experiment[33] on 6H-SiC gives different values of the second-harmonic susceptibilities which we find difficult to understand.

Bond-additivity, which is a basic assumption of the semiclassical models to predict the second-harmonic susceptibilities, is tested to work in some compounds (4H-SiC, 6H-SiC, and BN) but fails in others (2H-SiC, AlN, and GaN). Although bond-additivity gives a simple, and in many cases[21] good relations between the different components of the second-harmonic susceptibilities, it is not always reliable as shown by our calculations.

The nonlinear local-field correction to the second-harmonic susceptibility is demonstrated numerically to be half the linear local-field corrections. The total local-field corrections ranges between -21% to $+30\%$ among the semiconductors currently studied. There are three orders of local-field corrections of which only the first-order correction is important. The second- and third-order corrections give at most a 4% correction and can be safely ignored.

REFERENCES

1. Z. H. Levine and D. C. Allan, Phys. Rev. B **48**, 7783 (1993).
2. H. Zhong, Z. H. Levine, D. C. Allan, and J. W. Wilkins, Phys. Rev. B **48**, 1384 (1993).
3. W. G. Aulbur, Z. H. Levine, J. W. Wilkins, and D. C. Allan, Phys. Rev. B **51**, 10691 (1995).
4. For an overall review of our methods, see Z. H. Levine, Int. J. Quantum Chem. **S28**, 411 (1994).
5. D. R. Hamann, M. Schlüter, and C. Chiang, Phys. Rev. Lett. **43**, 1494 (1979); G. B. Bachelet, D. R. Hamann, and M. Schlüter, Phys. Rev. B **25**, 2103 (1982).
6. P. E. Blöchl, Phys. Rev. B **41**, 5414 (1990).
7. L. Kleinman and D. M. Bylander, Phys. Rev. Lett. **48**, 1425 (1982).
8. S. G. Louie, S. Froyen, and M. L. Cohen, Phys. Rev. B **26**, 1738 (1982).
9. For an excellent review on the pseudopotentials, see W. E. Pickett, Computer Physics Reports **9**, 115 (1989).
10. N. Troullier and J. L. Martins, Phys. Rev. B **43**, 1993 (1991).
11. X. Gonze, P. Käckell, and M. Scheffler, Phys. Rev. B **41**, 12264 (1990).
12. J. C. Slater, *The calculation of molecular orbitals*, (New York, Wiley, 1979), Chap. 2.
13. M. Rohlfing, P. Krüger, and J. Pollmann, Phys. Rev. B **48**, 17791 (1993).
14. M. P. Surh, S. G. Louie, and M. L. Cohen, Phys. Rev. B **43**, 9126 (1991).
15. A. Rubio, J. L. Corkill, M. L. Cohen, E. L. Shirley, and S. G. Louie, Phys. Rev. B **48**, 11810 (1993).
16. S. Strite, M. E. Lin, and H. Morkoc, Thin Solid Films **231**, 197 (1993).
17. M. Teter, Phys. Rev. B **48**, 5031 (1993).
18. J. Chen, Z. H. Levine, and J. W. Wilkins, Phys. Rev. B **50**, 11514 (1994).
19. Numerical Data and Functional Relationships in Science and Technology, edited by K.-H. Hellwege, Landolt-Bornstein Tables, Group III, Vol. 17a (Springer-Verlag, New York, 1982).
20. A. R. Verma and P. Krishna, *Polymorphism and polytypism in crystals*, (Wiley, New York, 1966), Chap. 5.
21. B. F. Levine, Phys. Rev. B **7**, 2600 (1973); Phys. Rev. Lett. **25**, 440 (1970).
22. F. N. H. Robinson, Phys. Lett. **26A**, 435 (1968).

23. S. Singh, J. R. Potopowicz, L. G. Van Uitert, and S. H. Wemple, Appl. Phys. Lett. **19**, 53 (1971). [Unknow SiC polytype]

24. H. Zhong, Z. H. Levine, D. C. Allan, and J. W. Wilkins, Phys. Rev. B **48**, 1384 (1993).

25. M. S. Hybertsen and S. G. Louie, Phys. Rev. B **35**, 5585 (1987).

26. M. S. Hybertsen and S. G. Louie, Phys. Rev. B **34**, 5390 (1986).

27. W. Godby, M. Schlüter, and L. J. Sham, Phys. Rev. B **37**, 10159 (1988).

28. M. Rohlfing, P. Krüger, and J. Pollmann, Phys. Rev. B **48,** 17791 (1993).

29. M.-Z. Huang and W.-Y. Ching, Phys. Rev. B **47**, 9449 (1993).

30. Y. Xu and W. Y. Ching, Phys. Rev. B **44**, 11048 (1991).

31. W. R. L. Lambrecht, B. Segall, W. Suttrop, M. Yoganathan, R. R. Devaty, W. J. Choyke, J. A. Edmond, J. A. Powell, and M. Alouani, Appl. Phys. Lett. **63**, 2747 (1993).

32. D. A. Kleinman, Phys. Rev. **126**, 1977 (1962).

33. P. M. Lundquist, W. P. Lin, G. K. Wong, M. Razeghi, J. B. Ketterson, Appl. Phys. Lett. **66**, 1883 (1995). [6H-SiC]

34. R. C. Miller, Appl. Phys. Lett. **5**, 17 (1964).

35. Z. H. Levine and D. C. Allan, Phys. Rev. B **44**, 12781 (1991); **48**, 14768 (E) (1993).

36. A. F. Wright and J. S. Nelson, Phys. Rev. B **50**, 2159 (1994).

37. M. P. Surh, S. G. Louie, and M. L. Cohen, Phys. Rev. B **43**, 9126 (1991).

38. A. Rubio, J. L. Corkill, M. L. Cohen, E. L. Shirley, and S. G. Louie, Phys. Rev. B **48**, 11810 (1993).

39. N. E. Christensen and I. Gorczyca, Phys. Rev. B **50**, 4397 (1994).

40. S. Nakamura, M. Senoh, N. Iwasa, S. Nagahama, T. Yamada, and T. Mukai, Jpn. J. Appl. Phys. **34**, L797 (1995); *ibid.* **34**, L1332 (1995).

41. S. Nakamura, M. Senoh, S. Nagahama, N. Iwasa, T. Yamada, T. Matsushita, H. Kiyoku, and Y. Sugimoto, Jap. J. Appl. Phys. Part 2-lett. v35, L74 (1996); v35, L217 (1996); Appl. Phys. Lett. **68**, 2105 (1996); **68**, 3269 (1996);

42. P. M. Lundquist, W. P. Lin, Z. Y. Xu, G. K. Wong, E. D. Rippert, J. A. Helfrich, and J. B. Ketterson, Appl. Phys. Lett. **65**, 1085 (1994).

43. W. P. Liu, P. M. Lundquist, G. K. Wong, E. D. Rippert, and J. B. Ketterson, Appl. Phys. Lett. **63**, 2875 (1993).

44. M. Alouani and J. Wills, unpublished.

45. Y. N. Xu and W. Y. Ching, Phys. Rev. B **48**, 4335 (1993).

46. Numerical Data and Functional Relationships in Science and Technology, edited by K.-H. Hellwege, Landoldt-Bornstein Tables, Group III, Vol. 17a (Springer-Verlag, New York, 1982).

47. A. T. Collins, E. C. Lightowlers, and P. J. Dean, Phys. Rev. **158**, 833 (1967).

48. L. Akasaki and M. Hashimoto, Solid State Commun. **5**, 851 (1967).

49. A. S. Barker and M. Ilegems, Phys. Rev. B **7**, 743 (1973).

50. Y. Fujii, S. Yoshida, S. Misawa, S. Maekawa, and S. Sakudo, Appl. Phys. Lett. **31**, 815 (1978). [AlN]

51. J. Miragliotta, D. K. Wickenden, T. J. Kistenmacher, and W. A. Bryden, J. Opt. Soc. Am. B, **10**, 1447 (1993). [GaN]

52. J. Miragliotta, private communication. [GaN]

53. H. J. Monkhorst and J. D. Pack, Phys. Rev. B **13**, 5188 (1976).